

Crystallographic Coalescence of Crystalline Silicon Clusters into Superlattice Structures

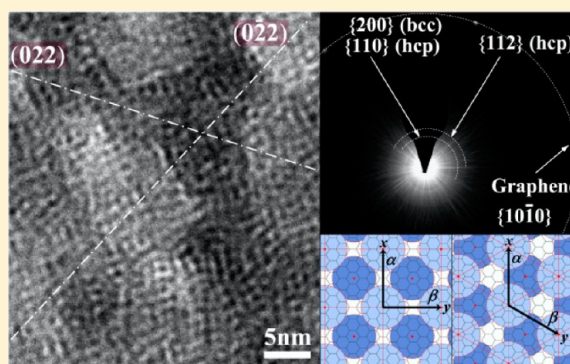
Yasushi Iwata,^{*,†} Kanako Tomita,[†] Takeyuki Uchida,[‡] and Hirofumi Matsuhata[§]

[†]Electronics and Photonics Research Institute, and [§]Advanced Power Electronics Research Center, National Institute of Advanced Industrial Science and Technology, Tsukuba Central 2, Tsukuba 305-8568 Japan

[‡]Research Institute for Ubiquitous Energy Devices, National Institute of Advanced Industrial Science and Technology, Osaka 563-8577, Japan

S Supporting Information

ABSTRACT: The crystallographic coalescence of crystalline silicon clusters into superlattice structures, generated by direct deposition of a silicon cluster beam on a graphene substrate, has been observed. High-resolution transmission electron microscopy and transmission electron diffraction analyses revealed that adjacent silicon clusters in the superlattices, having a mean diameter of 1.61 ± 0.05 nm ($n = 109$, n indicating the cluster size, Si_n) and an sp^3 diamond structure, form sp^3 covalent bonds between Si atoms on their surfaces and align their atomic crystalline axes, forming crystallographic rows to coalesce into bcc superlattice structures with a lattice constant of 2.134 ± 0.002 nm. The hcp configuration of the silicon clusters with the same lattice constant as the bcc superlattice unit cell is commensurate with the crystallographic structure of the graphene substrate. The absorption spectra confirm the sp^3 diamond structure of the silicon clusters under well-quantized conditions. Oxygen-free unoccupied electronic states (UDOS) in the conduction band of the silicon cluster superlattices appeared at 99.8 eV in the electron energy loss spectroscopy spectra. The $s + d$ UDOS at 107.5 eV in SiO_2 became conspicuous as the oxidation of the specimen advanced. The collective bulk plasmon loss of the virtually oxygen-free silicon cluster superlattice appeared at 16.7 eV.



INTRODUCTION

Three-dimensional ordered arrays that consist of crystalline silicon nanoparticles (e.g., silicon nanocrystals or silicon clusters in the gas phase) have received much attention in the last two decades, since the superlattice structure of silicon nanocrystals is characterized by collective electronic phenomena¹ that differ from the physical properties of isolated nanocrystals or bulk crystalline materials.^{2–4} Silicon-nanocrystal superlattices have had a significant impact on current developments in optoelectronics,^{5–7} quantum-dot photovoltaic cells,^{8–10} thermoelectrics,^{11,12} nanoelectronics,¹³ and biomaterials in vivo.^{14–16} These collective electronic properties result from the interactions between neighboring nanocrystals; the quantum states of the nanocrystal superlattices are then defined by a precisely controlled size of the nanocrystals as well as the interparticle distances. Dipole–dipole interactions between adjacent nanocrystals, which generate a dispersion potential as a van der Waals potential, play an important role in forming self-organized superlattice structures of colloidal nanocrystals. In systems characterized by such short-range interactions, the mechanism of nanocrystal ordering has been demonstrated to be well-described as a Kirkwood–Alder transition from a dispersion fluid to an ordered solid; this leads to the formation of a closed-packed face center cubic (fcc) or hexagonal closed-packed (hcp) configuration.^{17–19} If the distance between the

nanocrystals is reduced to less than 0.4 nm, the quantum mechanical wave functions of adjacent nanocrystals overlap, and silicon nanocrystal superlattices may form covalent valence bonds between the nanocrystals;¹⁰ as a result, the resonant charge transport may be significantly enhanced through mini-band channels, which are typically formed collective electronic states in superlattice structures. Thus, the investigation of the formation of these covalent valence bonds is fundamental to understand the dynamic transition in collective electron transport, such as a Mott–Hubbard transition, which depends on the strong coupling between adjacent nanocrystals^{19,20} as well as coalescence dynamics that is not confined to the formation of super molecules of nanocrystals, such as dimers, trimers, etc.,^{21,22} but also includes crystallographic coalescence into superlattice structures of nanocrystals. However, the crystallographic coalescence of colloidal nanocrystals into superlattice structures, characterized by covalent valence bonds, cannot be easily achieved, because their surfaces are coated with ligands (typically thiols), which are necessary to stabilize the superlattice structure, thereby sterically overcoming their propensity to agglomerate and sinter. These

Received: November 16, 2014

Published: March 12, 2015

ligands, however, cause a separation of the core nanocrystals to distances of a few nanometers or longer.²³

Silicon cluster superlattices, generated by deposition of ligand-free bare silicon clusters in the gas phase, are ideally suited to study the crystallographic coalescence into superlattices. A crystallographic approach to investigate the crystallographic coalescence into superlattices is necessary for at least three reasons: (1) It has been reported that isolated small silicon clusters ($200 > n \geq 30$, n indicating the cluster size, Si_n) cannot retain a sp^3 diamond structure, but form compact spherical-shaped sp^2 cage structures.^{24–26} Then, it is an important problem whether an sp^3 diamond structure is unstable even in a silicon cluster superlattice. (2) The crystallographic configuration of silicon clusters in a silicon cluster superlattice is closely related to the interaction potential, which makes the coupling of silicon clusters sufficiently strong to coalesce into superlattice structures. Besides a closed packed configuration (e.g., fcc or hcp structures), the formation of an unclosed-packed body-center cubic (bcc) structure is triggered by the strong interaction potentials.^{18,19,27} (3) A final reason to adopt a crystallographic approach is to investigate the interaction of silicon clusters with the substrate during the formation of the silicon cluster superlattice.

In this study, the crystallographic coalescence into silicon cluster superlattice structures has been investigated with the use of a new laser ablation-type silicon cluster beam system. This system, which is based on a principle that has been theoretically^{28–31} and empirically³² developed, can control the growth of the silicon clusters by shock-wave confinement to obtain a highly condensed pulsed beam with a uniform size distribution. Absolute values of the crystallographic structures of the silicon cluster superlattices formed on a graphene substrate were also studied and discussed to describe the crystallographic coalescence into the superlattice structure.

EXPERIMENTAL SECTION

All the experiments have been performed with a new laser ablation-type silicon cluster beam system. Silicon clusters were generated in an ellipsoidal-shaped cell with two focal points located at a distance of 78 mm, and with a major radius of 50 mm (Figure 1).

A silicon single crystal target with a cylindrical shape and diameter of 20 mm was set so that the ablation point was located at one of the focal points. The rotation speed of the target was controlled to avoid superheating conditions during the laser beam irradiation on the target surface. Helium, preserved in a circular-shaped reservoir, was continuously introduced into the cell through a narrow circular gap as a laminar flow with no turbulence. Both the circular reservoir and the cell were cooled down at liquid-nitrogen temperature. A pulsed beam of a multimode Nd:YAG laser ($\lambda = 532$ nm, Quantel) irradiated the target surface at a typical energy of 670 mJ per pulse for 12–13 ns at a repetition rate of 20 Hz. A condenser lens with a long focus (1500 mm) was set for the beam to focus on the point near the entrance window of the cell; the irradiation area on the target surface was adjusted to control the energy density deposited on the target surface below 9 J/cm^2 ,³³ so that the energy density was 5.3 J/cm^2 . The mean erosion rate of the silicon atoms was 2.66×10^{16} per laser shot; this was estimated from the reduction of the target weight. The beam profiles were measured with a CCD profile monitor set on two specific positions outside the vacuum, which resulted in equal distances from the condenser lens to the entrance window of the cell and to the target surface in the real vacuum system. Typical beam profiles are shown in Figure 1. A large number of silicon atoms ejected collectively in the direction perpendicular to the target surface and induced a shock in a static helium flow. A spherical shock wave, centered at the focal point on the target surface, was propagated and reflected on the wall of the cell; it was then focused on the other focal point near the exit of the

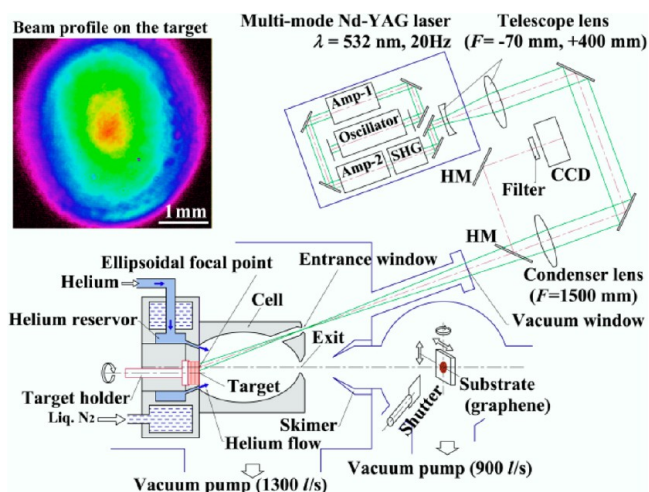


Figure 1. New laser ablation-type silicon cluster beam system; this consists of an ellipsoidal-shaped cell, a silicon single crystal target set at the focal point of the cell, a circular-shaped helium reservoir cooled at liquid-nitrogen temperature, a multimode Nd:YAG laser, and a CCD beam profiler. A pulsed neutral beam of silicon clusters generated in the spatiotemporal-confined cluster source is introduced via a skimmer into the synthesis chamber in a high vacuum below 1×10^{-7} Pa. The beam profile on the target surface is shown.

cell.²⁹ The reflected shock wave collided with the silicon vapor front traveling forward along the center axis of the cell; the silicon vapor front was stalled near the focal point.^{28,32} A thinner part of the hot silicon vapor front mixed with helium at liquid-nitrogen temperature; a dense mixed gas-phase layer was formed at the contact area of both gases. Silicon clusters were then generated in the mixed gas-phase layer, which was confined in a narrow space with a thickness smaller than 1.0 mm. Confinement of the mixed gas-phase layer, such that it lasted for a much shorter time (150–200 μs)³² than the time scale of diffusion (1 ms typical), allowed for uniform regulation of the thermodynamically adiabatic conditions; these are necessary to control the silicon cluster growth with a monodispersive cluster-size distribution. A group of silicon clusters, effusing from the exit of the cell into a vacuum, formed a pulsed neutral beam after passing through a skimmer; this was introduced into a synthesis chamber in a high vacuum (below 1×10^{-7} Pa). The silicon cluster beam was deposited on a graphene substrate.

Graphene substrates were generated by applying the chemical exfoliation method.^{34,35} After oxidation of natural graphite (SNO-15, purity 99.65%, mean diameter 20 μm , SEC Carbon Co. Ltd.) with the Hummer's reagent³⁶ (for details, see Supporting Information, section 1), a highly viscous solution of graphitic oxide was obtained. After dilution with a 5% sulfuric acid aqueous solution, a 30–35% hydrogen peroxide aqueous solution was added to stop the oxidation. The graphitic oxide solution was then purified in a mixed aqueous solution of 3% sulfuric acid and 0.5% hydrogen peroxide, and then in pure water. During purification, manganese and other ions were removed from the graphitic oxide, and thinner graphitic pieces were exfoliated from the graphitic oxide. Finally, graphitic crystals as thin as an atomic layer of graphene were floating and separated from the thick graphitic oxide in a centrifuge tube filled with a dispersion solution of isopropyl alcohol. A droplet of the dispersion solution was added on a microgrid with no backing foil; after drying, graphene films were obtained. The graphene substrate was sufficiently thin to obtain clear high-resolution transmission electron microscopy (HRTEM) images. The residual oxygen content in the graphene substrate was very small, i.e., less than 9.4% of the carbon element content; this was analyzed by energy dispersive X-ray spectroscopy (for further details, see Supporting Information, section 1). In this study, graphene is crucial to determine the absolute values of the lattice constants both in the atomic crystalline structure of silicon clusters and in the cluster superlattice

structures. Graphene possesses a hexagonal crystalline structure, which is characterized by the Miller-Bravais indices $\{hkl\}$, with $i = -(h + k)$. Before use, the lattice constant of graphene a_{graphene} was determined by transmission electron diffraction (TED) as³⁷

$$a_{\text{graphene}} = 0.24618 \pm 0.00025 \text{ nm} \quad (1)$$

This is consistent with the lattice constant of graphite (0.246172 nm; for further details, see Supporting Information, section 2).³⁸

High-resolution images and TED patterns of the silicon cluster superlattices were observed with a transmission electron microscope (TECNAI G2-F20, FEI) at 120 keV. Since silicon cluster superlattices possess substantial dual periodic potentials of the atomic crystalline structures and the crystallographic configuration of silicon clusters, illumination beams incident on a silicon cluster superlattice exhibit two types of TED patterns (for further details, see Supporting Information, section 3). To separate these two types of diffraction beams, besides the selected area aperture, an appropriate objective lens aperture was chosen from among the following fixed lens apertures: A1 (diameter of 10 μm), A2 (20 μm), A3 (40 μm), A4 (100 μm). The diffraction beam selection method is suitable for the analysis of the silicon cluster superlattice.^{39–42} All the diffracted beams from the periodic potentials of the atomic crystalline structures have to be intercepted for the residual diffracted beams from a silicon cluster superlattice to form conspicuous conjugate HRTEM images of the crystallographic configuration of the silicon clusters. The TECNAI G2-F20 is equipped with a magnetic energy analyzer ($\Delta E = 3 \text{ eV}$, 860 GIF2001, Gatan Inc.); highly resolved images can be obtained by selecting elastic beams. The mean depth resolution in the crystalline silicon was estimated to be 4.387 nm with the use of the energy loss data.⁴³ The high resolution in depth allows the analysis of the synthesized thick specimen of the silicon cluster superlattices. Importantly, the illumination beam at higher energies (e.g., 200 keV) caused serious damage of the graphene substrate.

Electron-energy loss spectroscopy (EELS) was performed during the scanning TEM (STEM) operation at 120 kV with a beam current below 0.1 nA, a beam size of 7 nm, and for 0.59–1.0 s. An energy resolution of $1.98 \pm 0.04 \text{ eV}$ in the full width at the half-maximum (fwhm) was obtained. EELS data were accumulated from several scanning square areas with a side of 200–400 nm.

Optical absorption spectra of silicon cluster superlattices synthesized on a glass substrate (OA-10G, Nippon Electric Glass Co. Ltd.) were collected with an absorption spectrophotometer (HSSP-1, Bunkoukeiki Co. Ltd.). The beam size was 1 mm^2 ; the wavelength resolution was 2 nm, in the wavelength range of 300 and 2000 nm.

RESULTS

Atomic crystalline structures of the silicon clusters deposited on the graphene substrate and consisting of silicon cluster superlattices were investigated. Figure 2 shows the TED patterns observed in an area of 0.5 μm in diameter of the specimen.

The Bragg's diffraction beams scattered from the atomic crystalline lattice of small silicon clusters formed peak maxima of ring patterns with broadened widths. The TED patterns also exhibited sharp single spots of graphene appearing simultaneously, suggesting that the graphene substrate consists of one single crystal in the observed area. Referring to the reciprocal lattice vector $G_{10\bar{1}0}$ diffracted from the graphene $\{10\bar{1}0\}$ planes, the reciprocal lattice vector R_{hkl} diffracted from the atomic crystalline lattice planes (hkl) in silicon clusters is given by

$$R_{hkl} = G_{10\bar{1}0} \frac{\sqrt{3}}{2} \frac{a_{\text{graphene}}}{a_{\text{Si}}} \sqrt{h^2 + k^2 + l^2} \quad (2)$$

where a_{graphene} is given by eq 1, and a_{Si} is the lattice constant of the atomic crystalline structure of the silicon clusters. Substituting the value $a_{\text{Si}} = 0.543095 \text{ nm}$,⁴⁴ corresponding to

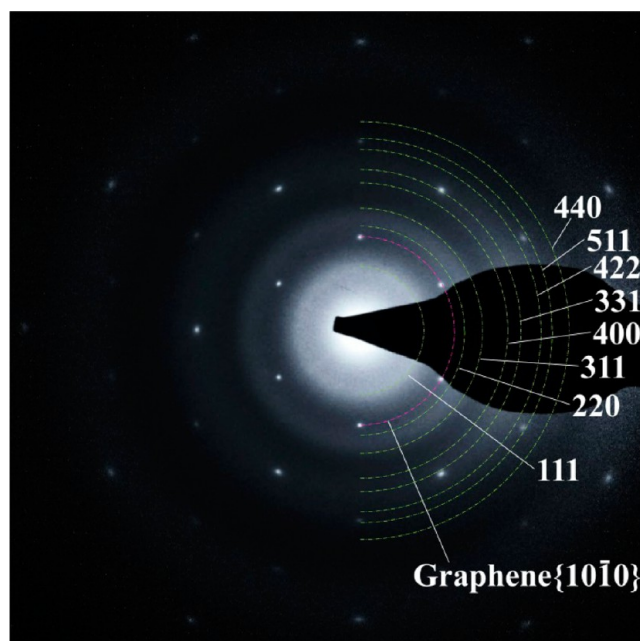


Figure 2. TED patterns at 120 kV of the silicon cluster superlattice formed on a graphene substrate. The observed area is a diameter of 0.5 μm on the specimen. The set of circles of the reciprocal lattice vectors R_{hkl} is defined in eq 2 by referring to the reciprocal lattice vector $G_{10\bar{1}0}$ of graphene. R_{hkl} is characterized by the Miller indices allowed for a diamond structure, i.e., $h + k + l = 4m$ and $4m \pm 1$ ($m = 1, 2, 3, \dots$).

the diamond structure of crystalline silicon, in eq 2 a set of reciprocal lattice vectors R_{hkl} are obtained that are characterized by the Miller indices allowed for a diamond structure, i.e., $h + k + l = 4m$ and $4m \pm 1$ ($m = 1, 2, 3, \dots$). As a result, the set of circles are well fitted to the observed ring patterns. Thus, the observed TED ring patterns of the atomic crystalline structures of the silicon clusters are consistent with a diamond structure with the same lattice constant as that of crystalline silicon.

The silicon cluster superlattice is characterized by substantial dual periodic potentials of atomic crystalline lattices and crystallographic configuration of silicon clusters. Since the atomic crystalline lattices in a silicon cluster mold have shorter periodic potentials than those in a cluster superlattice configuration, significantly more intense Bragg's diffraction beams were diffracted from the atomic crystalline lattice. Consequently, the conjugate HRTEM images with these Bragg's diffraction beams mainly originated from atomic crystalline lattices. Figure 3a shows the conjugate HRTEM images with Bragg's diffraction beams from the atomic crystalline structures of the silicon cluster superlattices.

The TED patterns of the Bragg's diffraction beams obtained without any objective lens aperture to intercept the Bragg's diffraction beams are shown in Figure 3b. The circles in Figure 3b indicate the reciprocal lattice vectors diffracted from graphene $\{10\bar{1}0\}$, which is then used in Figure 4b and Figure 5b as a reference.

The Fourier transform analysis (FTA) over an area of 38 nm \times 38 nm on the HRTEM images showed sharp ring patterns and some clear spots (Figure 3c). The FTA patterns are consistent with the reciprocal lattice vectors allowed for a diamond structure, which, according to eq 2, can be defined by the structure factors characterized by the condition $h + k + l = 4m$ and $4m \pm 1$ ($m = 1, 2, 3, \dots$). The spot patterns formed a symmetrical pair around the center, each line joining the pairing

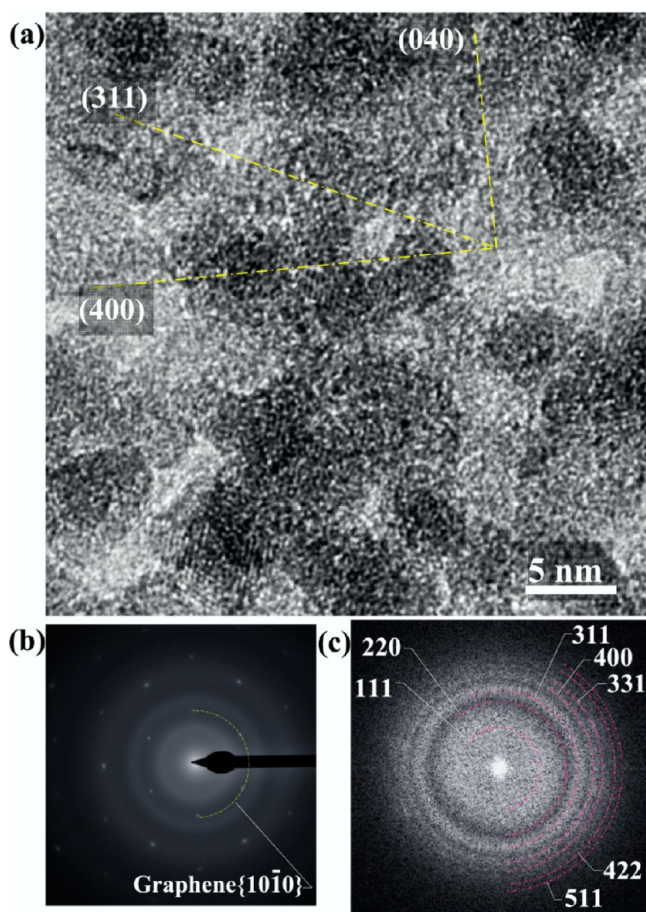


Figure 3. (a) The conjugate HRTEM images at 120 kV with the intense Bragg's diffraction beams from the atomic crystalline structures in the silicon cluster superlattice. (b) TED patterns of the intense Bragg's diffraction beams from the atomic crystalline structures obtained without any objective lens aperture. (c) FTA over an area of $38 \text{ nm} \times 38 \text{ nm}$ on the HRTEM images. A set of circles indicates the reciprocal lattice vectors allowed for a diamond structure, i.e., $h + k + l = 4m$ and $4m \pm 1$ ($m = 1, 2, 3, \dots$). The (311) and the (400) crystalline planes intersect each other at 25.2° .

spots being perpendicular to the individual atomic crystalline plane in the HRTEM images. The characteristic (311) and (400) planes that intersect each other at 25.2° are shown in Figure 3a.

The conjugate HRTEM images of the crystallographic configuration of silicon clusters in the silicon cluster superlattices were obtained when the intense Bragg's diffraction beams from the atomic crystalline lattice were intercepted by the objective lens apertures A3 (which allows a part of the Bragg's diffraction beams from the (111) atomic crystalline lattice planes to pass through and intercept the other diffraction beams with higher indices) and A2 (which intercepts all the Bragg's diffraction beams from the atomic crystalline lattice planes more rigorously). Interception of A3 and A2 is displayed on the TED patterns in Figure 4b and Figure 5b, respectively. The HRTEM images in Figure 4a, conjugate with the Bragg's diffraction beams intercepted by A3, consist of images of both the atomic crystalline structures and crystallographic configuration of the silicon clusters. The FTA patterns of the HRTEM images (Figure 4c) show no clear spot pattern. The conjugate HRTEM images with the Bragg's diffraction beams intercepted by A2 are shown in Figure 5a; here, the phase

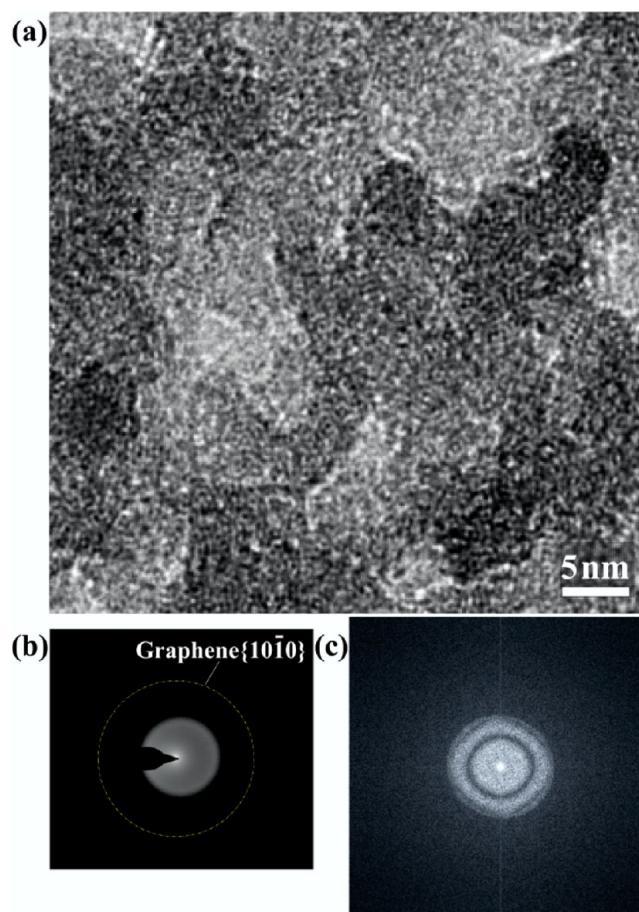


Figure 4. (a) The conjugate HRTEM images with the Bragg's diffraction beams, excluding the (111) atomic crystalline lattice planes and crystallographic cluster lattice arrays. (b) TED pattern of the Bragg's diffraction beams intercepted by the objective lens aperture A3. (c) FTA patterns of the HRTEM images.

contrast of the atomic crystalline structures completely disappears. As a result, among the dual periodic potentials, the characteristic longer one for the crystallographic configuration of silicon clusters clearly appeared. The conjugate HRTEM images revealed that the mean diameter of the silicon clusters is significantly smaller than 2.0 nm , with a monodispersive size distribution and a densely packed cluster superlattice structure. The FTA of the HRTEM images reveals spot patterns of the reciprocal lattice vectors 200, 211, 220, 310 (Figure 5c).

The crystallographic structures of the silicon cluster superlattices were further investigated quantitatively with TED. Figure 6a,b shows the observed TED ring-shaped patterns diffracted from the crystallographic planes of the silicon cluster superlattices, which appeared near the beam center (00 spot).

On the basis of the simultaneously observed reciprocal lattice vectors $G_{10\bar{1}0}$ of graphene, the reciprocal lattice vectors Λ_{uvw} in the TED patterns with the Miller indices (uvw) of the crystallographic configuration of silicon clusters can be used to empirically determine the absolute value of the lattice constant $\alpha_{\text{cluster-lattice}}$ in the cubic structure, as per the following equation

$$\alpha_{\text{cluster-lattice}} = a_{\text{graphene}} \frac{\sqrt{3} G_{10\bar{1}0}}{2 \Lambda_{uvw}} \sqrt{u^2 + v^2 + w^2} \quad (3)$$

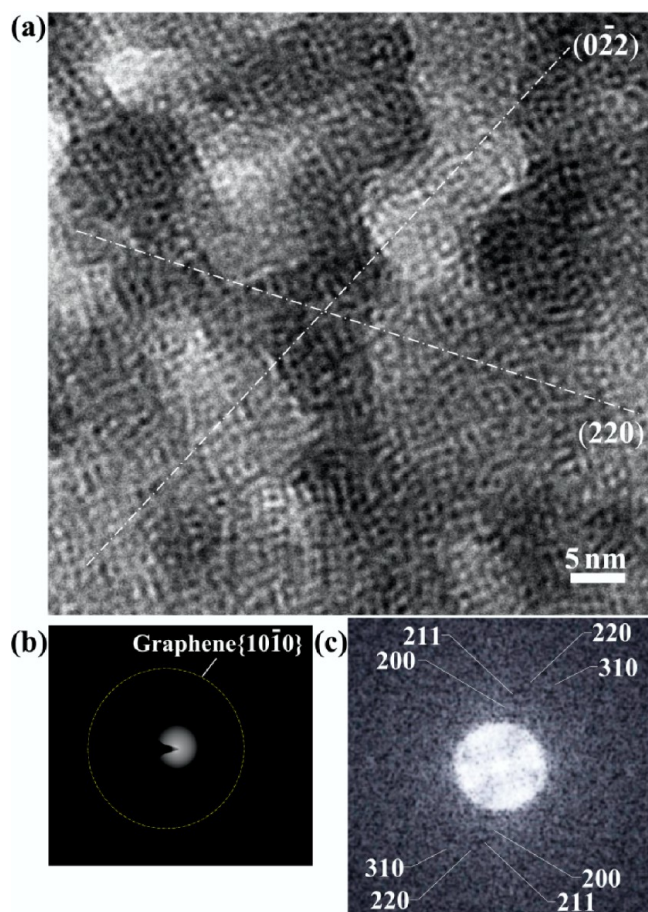


Figure 5. (a) The conjugate HRTEM images with the Bragg's diffraction beams intercepted by the objective lens aperture A2; the characteristic cluster superlattice arrays of a long period appear clearly. (b) TED pattern of the Bragg's diffraction beams intercepted by the objective lens aperture A2. (c) FTA patterns of the HRTEM images indicating spot patterns of the crystallographic (200), (211), and (220) superlattice planes of the silicon cluster superlattice.

where a_{graphene} is given by eq 1. A careful analysis of the values of $G_{10\bar{1}0}/\Lambda_{uvw}$ revealed that the superlattice structures possess intrinsic {200} and {211} planes, which yield the $\alpha_{\text{cluster-lattice}}$ values as summarized in Table 1. Finally, the lattice constant $\alpha_{\text{cluster-lattice}}$ in the cubic structure was determined with taking an average,

$$\alpha_{\text{cluster-lattice}} = 2.134 \pm 0.002 \text{ nm} \quad (4)$$

Since the {211} diffraction is uniquely allowed in the bcc structure, it can be proven that the silicon cluster superlattices can form a bcc superlattice structure. $\alpha_{\text{cluster-lattice}}$ defines a bcc unit cell to give densities of silicon clusters in the superlattice as $2.057 \times 10^{20} \text{ cm}^{-3}$ on average and $4.391 \times 10^{13} \text{ cm}^{-2}$ on every stacked layer. Notably, the ratio $G_{10\bar{1}0}/\Lambda_{uvw}$ gave integer numbers (i.e., 5.00), suggesting that the interspace distance of the {200} planes in the bcc cluster superlattice is precisely five times as large as that of the graphene $\{10\bar{1}0\}$ plane ($=\sqrt{3}a_{\text{graphene}}$). Figure 6c shows the crystallographic configuration of the silicon clusters that formed a bcc structure on the graphene substrate. The {200} planes are one-dimensionally (e.g., in the x -axis direction) commensurate with the crystallographic structure of graphene; any other crystallographic plane of the silicon clusters is not commensurate. Accordingly, the bcc configuration of the silicon clusters may be possibly formed

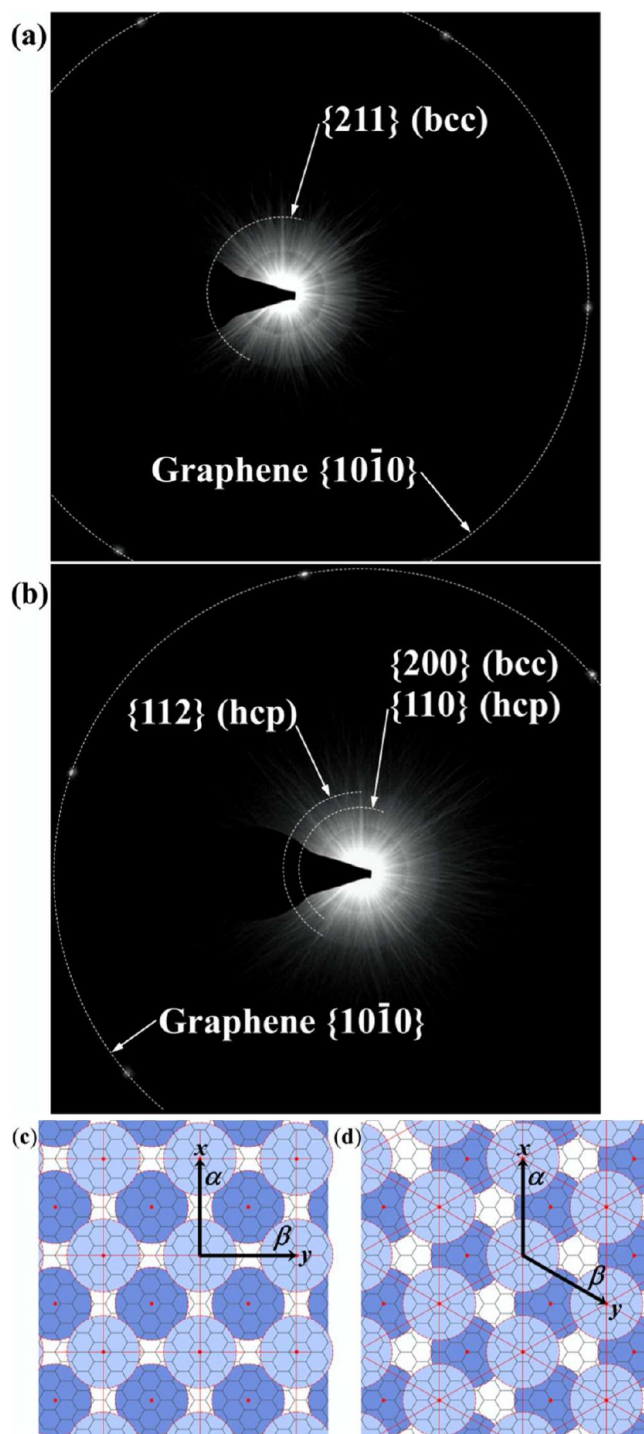


Figure 6. TED analysis of the crystallographic silicon cluster superlattices. (a, b) TED patterns deflected from cluster superlattice arrays appearing near the beam center (00 spot). The reciprocal lattice vectors $G_{10\bar{1}0}$ of graphene $\{10\bar{1}0\}$ are indicated as a reference to determine the absolute value of the lattice constant $\alpha_{\text{cluster-lattice}}$ of the silicon cluster superlattice. (c) Crystallographic configuration of the silicon clusters forming a bcc structure on the graphene substrate; {200} planes are one-dimensionally commensurate with the graphene $\{10\bar{1}0\}$ planes. (d) Hcp structure of silicon cluster configuration formed on the graphene substrate. All silicon clusters placed on lattice sites are commensurate with the crystallographic structure of graphene.

Table 1. Lattice Constant $\alpha_{\text{cluster-lattice}}$ of the Observed Silicon Cluster Superlattice Determined from eq 3 for the Cubic Structure (bcc), and from eq 5 for the Hexagonal Closed Packed Structure (hcp)

	$G_{10\bar{1}0}/\Lambda_{uvw}$	BCC		HCP		$\alpha_{\text{cluster-lattice}}$ [nm]
		$\{uvw\}$	$(\sqrt{3}/2) (u^2 + v^2 + w^2)^{1/2}$	$\{uvw\}$	$(\sqrt{3}/2) ((4/3) (u^2 + uv + v^2) + (9/16)w^2)^{1/2}$	
I	5.005	200	$\sqrt{3}$	110	$\sqrt{3}$	2.1361
II	5.00	200	$\sqrt{3}$	110	$\sqrt{3}$	2.134
	4.002			112	$5\sqrt{3}/4$	2.135
III	4.079	211	$3/\sqrt{2}$			2.132

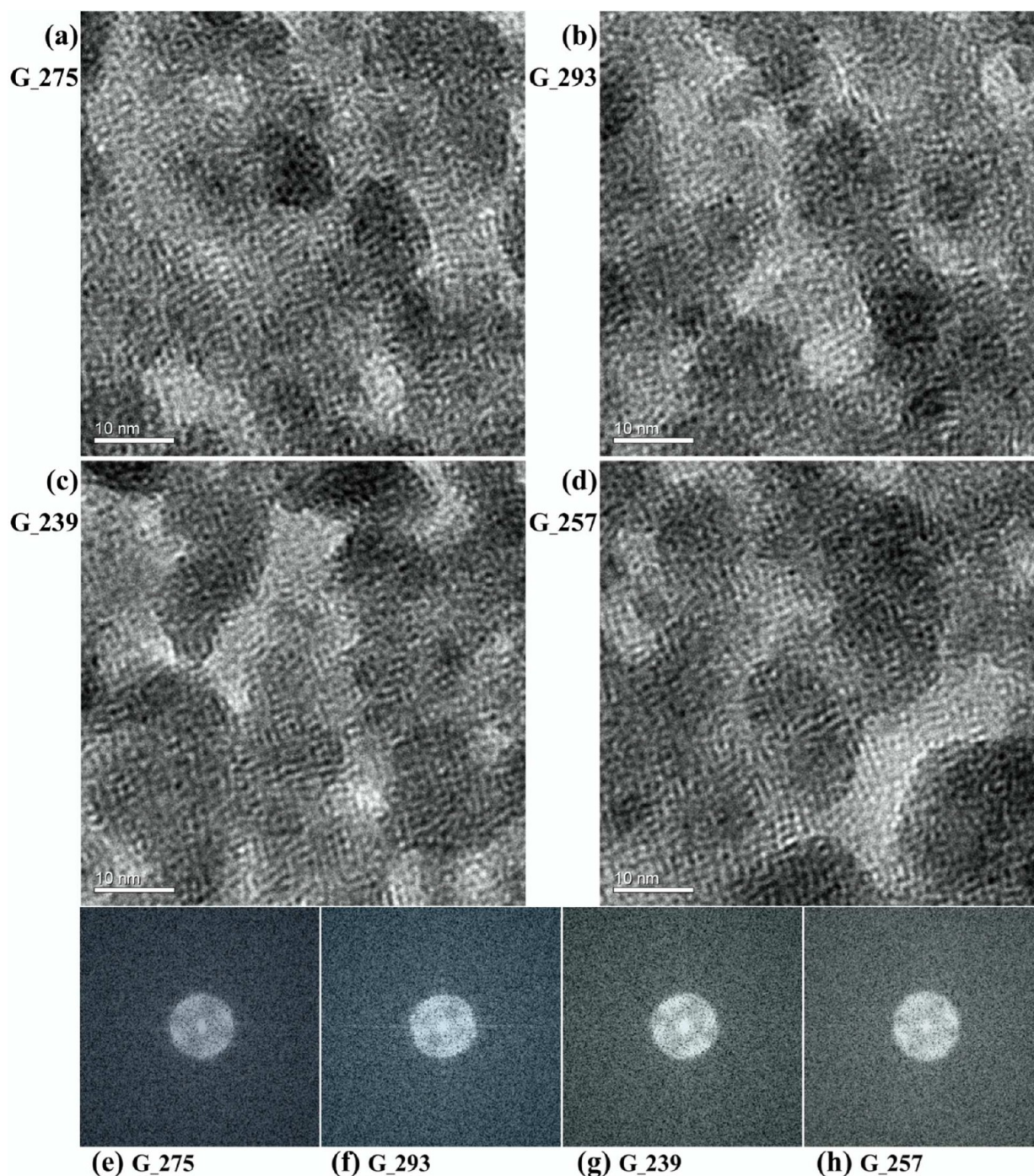


Figure 7. (a–d) The conjugate HRTEM images at 120 kV with the Bragg's diffraction beams intercepted by A2, in the selected areas on the silicon cluster superlattice. (e–h) FTA patterns corresponding to the individual HRTEM images.

in the silicon cluster superlattice independently of the crystallographic structure of the graphene substrate. Interest-

ingly, another solution of the superlattice structure, significantly more commensurate with graphene, has been obtained by

introducing an hcp configuration of silicon clusters. Assuming that the third lattice constant in the hcp configuration $\gamma_{\text{cluster-lattice}}$ is equal to $4/3\alpha_{\text{cluster-lattice}}$, eq 3 can be modified as follows:

$$\alpha_{\text{cluster-lattice}} = a_{\text{graphene}} \frac{\sqrt{3}}{2} \frac{G_{10\bar{1}0}}{\Lambda_{uvw}} \sqrt{\frac{4}{3}(u^2 + uv + v^2) + \frac{9}{16}\omega^2} \quad (5)$$

Two types of reciprocal lattice vectors defined by eq 5 from the $\{110\}$ and $\{112\}$ planes satisfied the empirical TED data $G_{10\bar{1}0}/\Lambda_{uvw}$ (Table 1). In particular, eq 5 revealed that the lattice constant $\alpha_{\text{cluster-lattice}}$ of the $\{110\}$ and $\{112\}$ planes in the hcp superlattice structure has the same value as that obtained from eq 4. Figure 6d shows the crystallographic configuration of silicon clusters forming an hcp structure on the graphene surface. All silicon clusters placed on the lattice sites commensurate with the crystallographic structure of graphene. Consequently, the hcp configuration of silicon clusters may be possibly formed in the initial stage of the synthesis of the silicon cluster superlattices depending on the crystallographic structure of the graphene substrate. The density of the silicon clusters in the hcp superlattice structure was determined to be $1.782 \times 10^{20} \text{ cm}^{-3}$ and $5.070 \times 10^{13} \text{ cm}^{-2}$ on every layer.

The HRTEM images of the silicon cluster superlattice shown in Figure 7a–d have been sampled in several areas of the specimen to confirm the bcc configuration, typical of the silicon cluster superlattices (Figure 6a,b). The FTA patterns of the individual HRTEM images are shown in Figure 7e–h. The spot patterns that appear in all the FTA patterns are characterized by 12 Miller indices (Figure 8a), all of which satisfy the condition

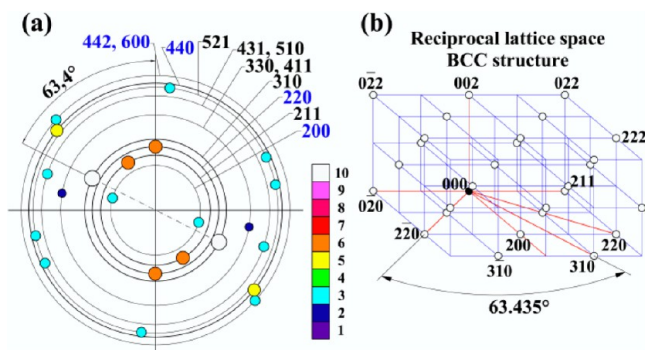


Figure 8. (a) Spot patterns appearing in the FTA patterns shown in Figure 7e–h. Characteristic Miller indices, 211, 310, 330/411, 431/510, 521 are typical of a bcc structure. The pairing 310 spots showed an extremely high intensity and appeared at 63.4° to the pairing 220 spots. (b) 310 axis in the bcc structure is at an angle of 63.435° to the 220 axis in the reciprocal lattice space.

of structure factors allowed for a bcc structure, i.e., $h + k + l = 2m$ ($m = 1, 2, 3, \dots$). In particular, seven of the Miller indices, namely, 211, 310, 330/411, 431/510, and 521 are characteristic of the bcc structure. The intensity of every spot pattern was determined by counting the number of appearance times of the same Miller indices. The pairing 310 spots showed an extremely high intensity; these appeared at an angle of 63.4° to the pairing 220 spots, whose value is consistent with the angle between the 310 axis and the 220 axis in the bcc structure in the reciprocal lattice space (Figure 8b). The results displayed

in Figure 8a confirm that silicon cluster superlattices possess a bcc structure with the lattice constant given in eq 4.

Figure 9 shows the absorption spectra of silicon clusters under relatively low-coverage synthesis conditions. Sharp

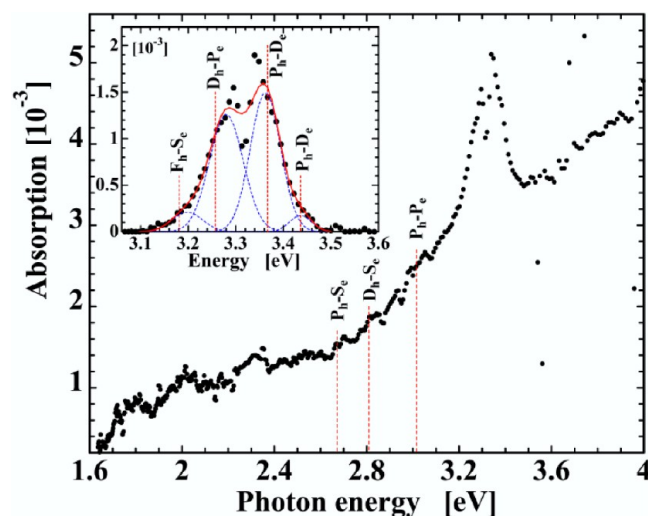


Figure 9. Absorption spectra of silicon clusters under relatively low-coverage synthesis conditions. Transitions P_h-S_e , D_h-S_e , P_h-P_e , and F_h-S_e , D_h-P_e , P_h-D_e shown in the inset were identified according to refs 10 and 45.

absorption peaks appearing at the energy range of 3.18 and 3.44 eV reveal that the electronic states in the silicon clusters are in a well-quantized confinement condition below 2 nm (Figure 5a). According to the numerically obtained spectra for isolated silicon clusters by Luo et al.¹⁰ and Melinon et al.,⁴⁵ the sharp absorption peaks may be identified as P_h-S_e , D_h-S_e , P_h-P_e , and F_h-S_e , D_h-P_e , P_h-D_e transitions as shown in the inset of Figure 9. The models of a diamond structure terminated by hydrogen have been used in these calculations; the electronic states could be drastically changed if some sp^2 states would be contained.⁴⁵ Accordingly, the present absorption experimental data support the sp^3 diamond structure of silicon clusters.

DISCUSSION

Direct deposition of bare silicon clusters in the gas phase is ideally suited to study the crystallographic coalescence into superlattice. Despite the experimental efforts to form a silicon cluster superlattice by direct deposition of silicon nanoparticles,^{7,46–48} only a few studies about ordered arrays of silicon nanoparticles have been reported.^{49,50} In the present study, the laser ablation-type silicon cluster beam system developed with a new principle of shock-confinement is crucial for the formation of the silicon cluster superlattices obtained by direct deposition of bare silicon clusters. In particular, a large amount of energy provided by the Nd:YAG laser was used to provide the kinetic energy to a large number of silicon atoms, which eject collectively from the target surface in every laser shot, i.e., 2.66×10^{16} silicon atoms with a kinetic energy of 90 eV/atom. The induced strong shock in the helium flow caused confinement of a thin mixed gas-phase layer compressed in a narrow volume (its thickness is smaller than 1.0 mm), where energetic silicon vapor molecules collide with dense helium at liquid-nitrogen temperature; thus, the silicon clusters are expected to show a dense growth and the mixed gas-phase to persist for 150–200 μs ;^{28,32} this period of time is significantly

shorter than 2–3 ms, typical of a pulse duration of a laser ablation cluster beam,⁵¹ and shorter than 1 ms, the typical time scale of diffusion in gas phase. This short period of confinement in a narrow space, referred to as “spatiotemporal confinement,” allows generating a high-peak particle current of a pulsed silicon cluster beam with a monodispersive size distribution. Assuming that the pulse duration of the present silicon cluster beam is 150 μ s, the peak current density is then 1.2×10^{16} cm⁻² s⁻¹, which corresponds to an incidence at every 6 μ s of silicon clusters striking a single domain area (38 nm \times 38 nm, Figure 3a) of silicon cluster coalescence. Previously deposited silicon clusters on the substrate may be collectively excited to rearrange their configuration by a single incidence of silicon clusters. Thus, a detailed study on the formation of the silicon cluster superlattices by direct deposition of bare silicon clusters is necessary.

The oxidation of silicon cluster superlattice has been investigated as a function of time, with the specimen being kept in a dry atmosphere in a desiccator. Figure 10 shows the EELS spectra obtained in the STEM operation at 120 kV. Measurements were thus performed within 1 day, after 26 days, and 167 days of deposition of silicon clusters. The Si L_{2,3} edges, corresponding to a transition from the Si 2p core state to the unoccupied conduction bands formed in the silicon cluster superlattice, are shown in Figure 10a. The edge onset A increases at an energy of 99.8 eV, which has been identified as the Si L_{2,3} edge of monocrystalline silicon.^{52,53} The edges A₁ ~ A₃ of the three major components of the unoccupied density of states (UDOS) of monocrystalline bulk silicon calculated by Batson and Heath⁵² are shown in the inset of Figure 10. The energies of the first EELS peak with the edge onset A are in good agreement with the edges of the three components. Accordingly, the first EELS peak with the edge onset A represents the UDOS of the oxygen free silicon cluster superlattice. No significant blue shift of the Si L_{2,3} edge onset A under the quantum confinement effects of silicon clusters was observed; however, Batson and Heath⁵² and Sun et al.⁵³ reported a blue shift of the Si L_{2,3} edge of Si nanoparticles and Si nanowires, respectively. The first EELS peak with the edge onset A completely disappeared as the oxidation of the specimen proceeded for 167 days. In contrast, the Si L_{2,3} edges onset B that become conspicuous with the advancement of the oxidation increase to an energy of 107.5 eV, which corresponds to a transition from the Si 2p core state to the s + d UDOS formed in SiO₂.^{53–56} The edge B₁ of the s-dominant states and the edge B₂ of the s + d states calculated by Garvie and Buseck⁵⁵ are shown in the inset of Figure 10. A sharp edge onset B* was found at 105.4 eV in the initial stage after synthesis of the silicon cluster superlattice and disappeared after a long lapse of 167 days. The Si L_{2,3} edges onset B align at the same energy as the oxidation proceeds. The plasmon-loss spectra have been observed in the low-energy-loss EELS region (Figure 10b); these data are normalized to the peak value of each zero-loss spectrum. The broad EELS peak A at an energy of 16.7 eV appearing in the initial stage after synthesis of the silicon cluster superlattice is in good agreement with the bulk plasmon loss of monocrystalline silicon.⁵⁷ Thus, the EELS peak suggests a collective bulk plasmon loss of the virtually oxygen free silicon cluster superlattice. Some energy-loss components of the surface plasmon in the superlattice appearing at 12 eV and a plasmon excitation confined in the silicon clusters appearing at 9 eV may broaden the peak in the low-energy

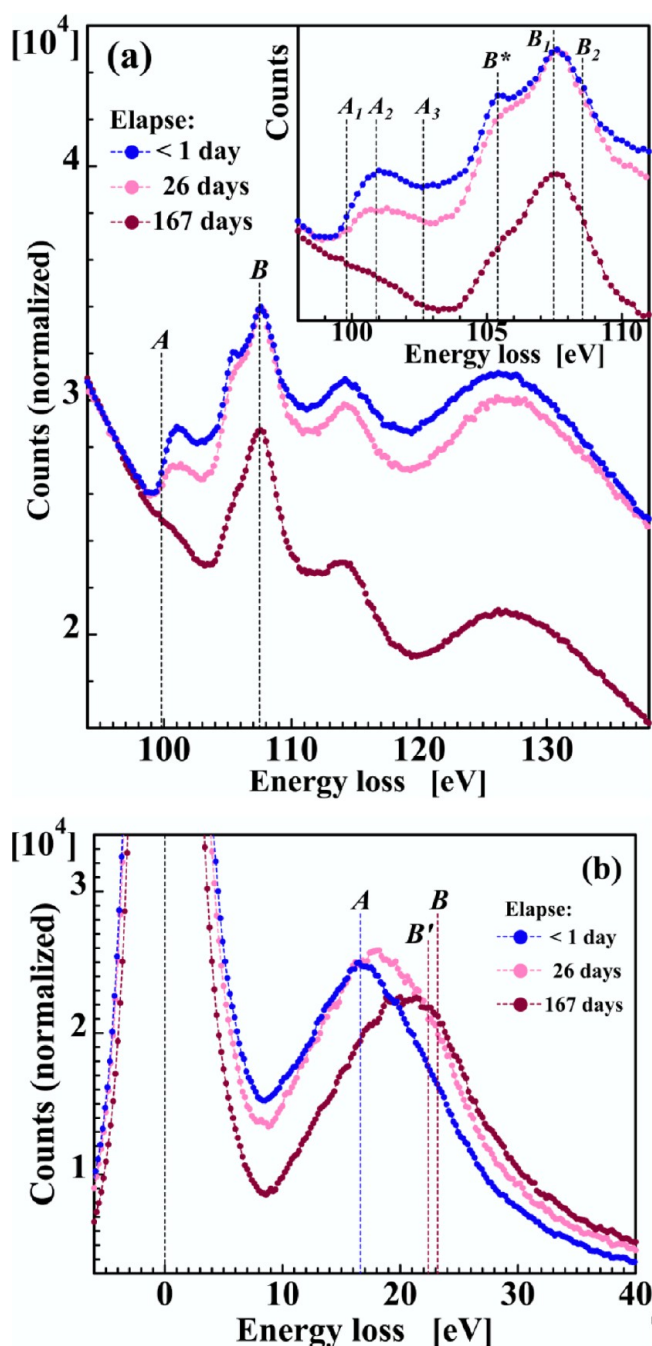


Figure 10. Time-lapse EELS spectra showing the oxidation of silicon cluster superlattice obtained in the STEM operation at 120 kV. (a) The Si L_{2,3} edge onset A reflects the UDOS in oxygen free of the silicon cluster superlattice. The edges A₁ ~ A₃ in the inset indicate the calculated UDOS of monocrystalline silicon.⁵² The Si L_{2,3} edge onset B reflects the s + d UDOS formed in SiO₂. The edges B₁ and B₂ in the inset indicate the calculated s-dominant states and the s + d states, respectively.⁵⁵ (b) Plasmon-loss spectra normalized to the peak value of each zero-loss spectrum. The broad EELS peak A appearing in the initial stage indicates the collective bulk plasmon loss of the virtually oxygen-free silicon cluster superlattice. The broader EELS peak B and B' indicate the plasmon states as oxidation proceeded for a long period of time.

area.⁵⁸ Another plasmon loss peak with an even broader width appeared at higher energies as the oxidation of the specimen advanced. The peak position, however, was located at a lower energy than that of the well-known plasmon-loss of SiO₂ or SiO

indicated as B and B', respectively.^{54,57} The plasmon-loss spectra measured during the oxidation of the specimen revealed that the collective bulk plasmon of the silicon cluster superlattice, initially in almost oxygen-free states, changes into plasmon states as the oxidation advanced after a long lapse of 167 days. Consequently, the crystallographic structure of the silicon cluster superlattice can be investigated with HRTEM and TED on specimens that have been exposed to air for less than 1 day after synthesis.

The results based on TED (Figure 2), FTA (Figure 3c), and absorption spectra (Figure 9) support the conclusion that the atomic crystalline structure of every silicon cluster forming the silicon cluster superlattices retains a sp^3 diamond structure with the same lattice constant as that of monocrystalline or polycrystalline silicon; however, isolated silicon clusters cannot retain a sp^3 diamond structure if the cluster size is smaller than 2 nm (Si_n , $200 > n \geq 30$).²⁴ Crystallographic transitions occurring at a cluster size $n = 30$ from a prolate shape ($30 > n$) to a compact spherical shape ($n \geq 30$) have been experimentally found in isolated silicon clusters.^{59,60} Several theoretical studies have suggested that the compact spherical shape possesses stable sp^2 cage structures.^{24–26} Unlike the fullerene symmetric cage structure of carbon clusters, the sp^2 cage structure of silicon clusters may have different crystallographic symmetries depending on the cluster size. This complicates the determination of the crystallographic structure of the silicon cluster superlattice in case the silicon clusters form isomeric sp^2 cage structures. However, our results showed that the sp^3 diamond structure of silicon clusters is stable in the silicon cluster superlattices. Even if the isolated silicon clusters generated in the cluster source had sp^2 cage structures, dynamic crystallographic transitions would occur during the formation of the superlattice structures on the substrate. Consequently, the isomer-free sp^3 diamond structure of every silicon cluster in the silicon cluster superlattices renders the analysis of the chemical structures of the silicon cluster superlattice independent of the cluster size.

The present results confirmed the unclosed-packed bcc structure of the silicon cluster superlattices, suggesting a strong coupling between adjacent silicon clusters.^{18,19,27} The spot patterns observed with FTA (Figure 3c) indicated that the sp^3 diamond structure is uniquely formed over an area of $38 \text{ nm} \times 38 \text{ nm}$ of the silicon cluster superlattice layers; 317 bcc unit superlattice cells were found, i.e., 634 silicon clusters collectively aligned their atomic crystalline axes to form crystallographic rows of the silicon cluster superlattice. Adjacent silicon clusters should be located in close proximity to form sp^3 covalent bonds between the Si–Si atoms on the surface, this leading to crystallographic coalescence of silicon clusters into superlattice structures. The face-to-face separation (FTFS) between the nearest-neighbor silicon clusters in the silicon cluster superlattice can be determined by the Si–Si covalent bond (0.235167 nm). Thus, taking into account the inter-distance $\alpha_{\text{cluster-lattice}} \sqrt{3}/2$ between the nearest-neighbor silicon clusters on the 110 closed-packed plane in the bcc superlattice unit cell, the mean diameter of the silicon clusters was determined to be $1.61 \pm 0.05 \text{ nm}$ ($n = 109$, n indicating the cluster size, Si_n). Notably, the so-determined FTFS is independent of n , unlike the lattice constant $\alpha_{\text{cluster-lattice}}$. Accordingly, the FTFS between the nearest neighbor silicon clusters acts as a new n -independent invariant in the silicon cluster superlattices.

CONCLUSIONS

In this study, we have observed the crystallographic coalescence of silicon clusters into superlattice structures; these were generated by direct deposition on a graphene substrate with a laser ablation-type silicon cluster beam system developed with a new principle of spatiotemporal confinement. The silicon clusters possess a monodispersive size distribution with a mean diameter of $1.61 \pm 0.05 \text{ nm}$ (for $n = 109$, n indicating the cluster size, Si_n) and retain a sp^3 diamond structure with the same lattice constant as that of monocrystalline silicon.

The silicon cluster superlattice shows an unclosed-packed bcc structure formed by a suitable configuration of the silicon clusters. The lattice constant $\alpha_{\text{cluster-lattice}}$ of the observed bcc superlattice unit cell is $2.134 \pm 0.002 \text{ nm}$. The density of silicon clusters in the superlattice is $2.057 \times 10^{20} \text{ cm}^{-3}$ on average, and $4.391 \times 10^{13} \text{ cm}^{-2}$ on every stacked layer.

Adjacent silicon clusters in the silicon cluster superlattice form sp^3 covalent bonds between the Si–Si atoms on the surfaces and align their atomic crystalline axes to form crystallographic rows of silicon cluster superlattices over a square area with a side of several tens nanometer.

The hcp configuration of the silicon clusters is commensurate with the crystallographic structure of the graphene substrate. The lattice constant $\alpha_{\text{cluster-lattice}}$ of the observed hcp superlattice unit cell is the same as that of the bcc superlattice unit cell. The density of silicon clusters in the hcp superlattice structure is $1.782 \times 10^{20} \text{ cm}^{-3}$ and $5.070 \times 10^{13} \text{ cm}^{-2}$ on every layer.

The absorption spectra of the silicon clusters under the relatively low-coverage synthesis conditions confirm their sp^3 diamond structure; the electronic states are in a well-quantized condition.

In addition, we have investigated the effects of oxidation as a function of time on the silicon cluster superlattices exposed to air. The UDOS of the oxygen-free silicon cluster superlattices appears in the EELS spectra with the edge onset at 99.8 eV. This completely disappears, and the $s + d$ UDOS in SiO_2 becomes conspicuous with the edge onset at 107.5 eV as the oxidation of the specimen advanced. The collective bulk plasmon loss of the virtually oxygen-free cluster superlattice results in an EELS peak at 16.7 eV.

To reveal the most significant features of the silicon cluster superlattices, further studies on the crystallographic coalescence of the crystalline silicon clusters into superlattice structures are currently performed in our laboratory.

ASSOCIATED CONTENT

Supporting Information

Graphene substrate; lattice constant of graphene; selected electron diffraction in HRTEM; references. This material is available free of charge via the Internet at <http://pubs.acs.org>.

AUTHOR INFORMATION

Corresponding Author

*Phone: +81-29-861-5750. Fax: +81-29-861-5320. E-mail: y.iwata@aist.go.jp.

Notes

The authors declare no competing financial interest.

ACKNOWLEDGMENTS

The authors thank Dr. O. Nakagawara, Dr. K. Murayama, Prof. M. Yaga, Dr. T. Takiya, Prof. P. Milani, Prof. M. Han for

discussion, Dr. M. Hirata and Dr. S. Horiuchi (for their support on the preparation of graphene), and Dr. K. Kawasaki (for his support on the HRTEM experiments). This work was supported by the cooperative research program of AIST and Murata Manufacturing Co., Ltd.

REFERENCES

- (1) Takagahara, T. *Surf. Sci.* **1992**, 267, 310–314.
- (2) Mangolini, L. *J. Vac. Sci. Technol., B* **2013**, 31, 20801.
- (3) Mastronardi, M. L.; Hennrich, F.; Henderson, E. J.; Maier-Flaig, F.; Blum, C.; Reichenbach, J.; Lemmer, U.; Kübel, C.; Wang, D.; Kappes, M. M.; Ozin, G. A. *J. Am. Chem. Soc.* **2011**, 133, 11928–11931.
- (4) Yu, Y.; Bosoy, C. A.; Hessel, C. M.; Smilgies, D. M.; Korgel, B. A. *ChemPhysChem* **2013**, 14, 84–87.
- (5) Pavesi, L.; Negro, L. D.; Mazzoleni, C.; Franzò, G.; Priolo, F. *Nature* **2000**, 408, 440–444.
- (6) Kúsova, K. *J. Non-Cryst. Solids* **2012**, 358, 2130–2133.
- (7) Ehbrecht, M.; Kohn, B.; Huisken, F. *Phys. Rev. B* **1997**, 56, 6958–6964.
- (8) Hao, X. J.; Cho, E. C.; Scardera, G.; Shen, Y. S.; Bellet-Amalric, E.; Bellet, D.; Conibeer, G.; Green, M. A. *Sol. Energy Mater. Sol. Cells* **2009**, 93, 1524–1530.
- (9) Löper, P.; Müller, R.; Hiller, D.; Barthel, T.; Malguth, E.; Janz, S.; Goldschmidt, J. C.; Hermle, M.; Zacharias, M. *Phys. Rev. B* **2011**, 84, 195317.
- (10) Luo, J. W.; Stradins, P.; Zunger, A. *Energy Environ. Sci.* **2011**, 4, 2546–2557.
- (11) Lin, K. H.; Strachan, A. *Phys. Rev. B* **2013**, 87, 115302.
- (12) Gillet, J. N.; Volz, S. J. *Electron. Mater.* **2010**, 39, 2154–2161.
- (13) Stafford, C. A.; Sarma, S. D. *Phys. Rev. Lett.* **1994**, 72, 3590–3593.
- (14) Low, S. P.; Voelcker, N. H.; Canham, L. T.; Williams, K. A. *Biomaterials* **2009**, 30, 2873–2880.
- (15) Liu, J.; Erogbogbo, F.; Yong, K. T.; Ye, L.; Liu, J.; Hu, R.; Chen, H.; Hu, Y.; Yang, Y.; Yang, J.; Roy, I.; Karker, N. A.; Swihart, M. T.; Prasad, P. N. *ACS Nano* **2013**, 7, 7303–7310.
- (16) Erogbogbo, F.; Yong, K. T.; Hu, R.; Law, W. C.; Ding, H.; Chang, C. W.; Prasad, P. N.; Swihart, M. T. *ACS Nano* **2010**, 4, 5131–5138.
- (17) Korgel, B. A.; Fullam, S.; Connolly, S.; Fitzmaurice, D. *J. Phys. Chem. B* **1998**, 102, 8379–8388.
- (18) Korgel, B. A.; Fitzmaurice, D. *Phys. Rev. B* **1999**, 59, 14191–14201.
- (19) Pileni, M. P. *J. Phys. Chem. B* **2001**, 105, 3358–3371.
- (20) Markovich, G.; Collier, C. P.; Henrichs, S. E.; Remacle, F.; Levine, R. D.; Heath, J. R. *Acc. Chem. Res.* **1999**, 32, 415–423.
- (21) van Huis, M. A.; Kunneman, L. T.; Overgaag, K.; Xu, Q.; Pandraud, G.; Zandbergen, H. W.; Vanmaekelbergh, D. *Nano Lett.* **2008**, 8, 3959–3963.
- (22) Dhakal, S.; Kohlstedt, K. L.; Schatz, G. C.; Mirkin, C. A.; de la Cruz, M. O. *ACS Nano* **2013**, 7, 10948–10959.
- (23) Yu, X.; Lei, D. Y.; Amin, F.; Hartmann, R.; Acuna, G. P.; Martínez, A. G.; Maier, S. A.; Tinnfeld, P.; Romero, S. C.; Parak, W. J. *Nano Today* **2013**, 8, 480–493.
- (24) Yu, D. K.; Zhang, R. Q.; Lee, S. T. *Phys. Rev. B* **2002**, 65, 245417.
- (25) Ho, K. M.; Shvartsburg, A. A.; Lu, B. P. Z. Y.; Wang, C.-Z.; Wacker, J. G.; Fye, J. L.; Jarrold, M. F. *Nature* **1998**, 392, 582–585.
- (26) Yoo, S.; Shao, N.; Zeng, X. C. *J. Chem. Phys.* **2008**, 128, 104316.
- (27) Wang, Z.; Schliehe, C.; Bian, K.; Dale, D.; Bassett, W. A.; Hanrath, T.; Klinke, C.; Weller, H. *Nano Lett.* **2013**, 13, 1303–1311.
- (28) Han, M.; Gong, Y.; Zhou, J.; Yin, C.; Song, F.; Muto, N.; Takiya, T.; Iwata, Y. *Phys. Lett. A* **2002**, 302, 182–189.
- (29) Yaga, M.; Takiya, T.; Iwata, Y. *Shock Waves* **2005**, 14, 403–411.
- (30) Weaver, K. E.; Lakhtakia, A. *Optik* **2008**, 119, 276–285.
- (31) Sayle, D. C.; Seal, S.; Wang, Z.; Mangili, B. C.; Price, D. W.; Karakoti, A. S.; Kuchibhatla, S. V. T. N.; Hao, Q.; Möbus, G.; Xu, X.; Sayle, T. X. T. *ACS Nano* **2008**, 2, 1237–1251.
- (32) Iwata, Y.; Kishida, M.; Muto, M.; Yu, S.; Sawada, T.; Fukuda, A.; Takiya, T.; Komura, A.; Nakajima, K. *Chem. Phys. Lett.* **2002**, 358, 36–42.
- (33) Takahashi, Y.; Muto, M.; Mital, S.; Iwata, Y. In *Proceedings of the 26th Annual Meeting of The Laser Society of Japan*; Oomiya, Japan, February 2, 2006.
- (34) Hirata, M.; Gotou, T.; Horiuchi, S.; Fujiwara, M.; Ohba, M. *Carbon* **2004**, 42, 2929–2937.
- (35) Horiuchi, S.; Gotou, T.; Fujiwara, M.; Sotoaka, R.; Hirata, M.; Kimoto, K.; Asaka, T.; Yokosawa, T.; Matsui, Y.; Watanabe, K.; Sekita, M. *Jpn. J. Appl. Phys.* **2003**, 42, L1073–L1076.
- (36) Hummers, W. S.; Offeman, R. E. *J. Am. Chem. Soc.* **1958**, 80, 1339–1339.
- (37) Iwata, Y.; Tomita, K.; Matsuhata, H. *Abstract of 2009 Annual Meeting of The Physical Society Japan*, Tokyo, March 28, 2009; 64–1, pp 828.
- (38) Howe, J. Y.; Rawn, C. J.; Jones, L. E.; Ow, H. *Powder Diffraction* **2003**, 18, 150–154.
- (39) Heidenreich, R. D. *Fundamentals of Transmission Electron Microscopy*; John Wiley and Sons, Inc.: New York, 1964.
- (40) Bernal, J. D. *Nature* **1928**, 122, 54.
- (41) Amelinckx, S.; Tendeloo, G. V.; Landuyt, J. V. *Bull. Mater. Sci.* **1984**, 6, 417–452.
- (42) Wang, Z. L. *J. Phys. Chem. B* **2000**, 104, 1153–1175.
- (43) Berger, M. J.; Coursey, J. S.; Zucker, M. A.; Chang, J. *NIST Physical Reference Data*, Ver. 1. 2. 3; National Institute of Standards and Technology: Gaithersburg, MD, 2005.
- (44) Pearson, W. B. *A Handbook of Lattice Spacings and Structures of Materials and Alloys Vol. 1*; Pergamon Press: Oxford, 1958.
- (45) Mélinon, P.; Kéghélian, P.; Prével, B.; Perez, A.; Guiraud, G.; Lebrusq, J.; Lermé, J.; Pellarin, M.; Broyer, M. *J. Chem. Phys.* **1997**, 107, 10278–10287.
- (46) Goldstein, A. N. *Appl. Phys. A: Mater. Sci. Process.* **1996**, 62, 33–37.
- (47) Mélinon, P.; Kéghélian, P.; Prével, B.; Dupuis, V.; Perez, A.; Champagnon, B.; Guyot, Y.; Lermé, M. P. J.; Broyer, M.; Rousset, J. L.; Delichère, P. *J. Chem. Phys.* **1998**, 108, 4607–4613.
- (48) Honda, Y.; Takei, M.; Ohno, H.; Shida, S.; Goda, K. *J. Lumin.* **2005**, 113, 279–284.
- (49) Sato, S.; Yamamoto, N.; Yao, H.; Kimura, K. *Chem. Phys. Lett.* **2002**, 365, 421–426.
- (50) Hofmeister, H.; Huisken, F.; Kohn, B. *Eur. Phys. J. D* **1999**, 9, 137–140.
- (51) Saito, N.; Iwata, Y.; Koyama, K.; Kitamura, T.; Tanimoto, M. *Surf. Rev. Lett.* **1996**, 3, 161–166.
- (52) Batson, P. E.; Heath, J. R. *Phys. Rev. Lett.* **1993**, 71, 911–914.
- (53) Sun, X.-H.; Tang, Y.-H.; Zhang, P.; Naftel, S. J.; Sammynaiken, R.; Sham, T. K. *J. Appl. Phys.* **2001**, 90, 6379.
- (54) Wang, J.; Wang, X. F.; Li, Q.; Hryciw, A.; Meldrum, A. *Philos. Mag.* **2007**, 87, 11–27.
- (55) Garvie, L. A. J.; Buseck, P. R. *Am. Mineral.* **1999**, 84, 946–964.
- (56) Garvie, L. A. J.; Rez, P.; Alvarez, J. R.; Buseck, P. R.; Craven, A. J.; Brydson, R. *Am. Mineral.* **2000**, 85, 732–738.
- (57) Tarrio, C.; Schnatterly, S. E. *J. Opt. Soc. Am. B* **1993**, 10, 952–957.
- (58) Berbezier, I.; Martin, J. M.; Bernardi, C.; Derrien, J. *Appl. Surf. Sci.* **1996**, 102, 417–422.
- (59) Jarrold, M. F.; Constant, V. A. *Phys. Rev. Lett.* **1991**, 67, 2994–2997.
- (60) Bachels, T.; Schafer, R. *Chem. Phys. Lett.* **2000**, 324, 365–372.